ACS NANO
Cite This: ACS Nano 2019, 13, 3457−3465
www.acsnano.org

ARTICLE

Surface Recombination in Ultra-Fast Carrier Dynamics of Perovskite Oxide $La_{0.7}Sr_{0.3}MnO_3$ Thin Films

Saeed Yousefi Sarraf,[†] Sobhit Singh,[†,‡] Andrés Camilo Garcia-Castro,[§] Robbyn Trappen,[†] Navid Mottaghi,[†] Guerau B. Cabrera,[†] Chih-Yeh Huang,[†,∥] Shalini Kumari,[†] Ghadendra Bhandari,[†] Alan D. Bristow,[†] Aldo H. Romero,*[,†] and Mikel B. Holcomb*[,†]

[†]Department of Physics and Astronomy, West Virginia University, Morgantown, West Virginia 26501-6315, United States
[‡]Department of Physics and Astronomy, Rutgers University, Piscataway, New Jersey 08854-8019, United States
[§]Department of Physics, Universidad Industrial de Santander, Cra. 27 Cll. 9, Bucaramanga, Colombia
[∥]Department Mechanical and Aerospace Engineering, West Virginia University, Morgantown, West Virginia 26501-6315, United States

Supporting Information

Aspects of the optoelectronic performance of thin-film ferromagnetic materials are evaluated for application in ultrafast devices. Dynamics of photocarriers and their associated spin polarization are measured using transient reflectivity (TR) measurements in cross linear and circular polarization configurations for $La_{0.7}Sr_{0.3}MnO_3$ films with a range of thicknesses. Three spin-related recombination mechanisms have been observed for thicker films (thickness of $d \geq 20$ nm) at different time regimes (τ), which are attributed to the electron−phonon recombination ($\tau < 1$ ps), phonon-assisted spin−lattice recombination ($\tau \sim 100$ ps), and thermal diffusion and radiative recombination ($\tau > 1$ ns). Density functional theory (DFT+U) based first-principles calculations provide information about the nature of the optical transitions and their probabilities for the majority and the minority spin channels. These transitions are partly responsible for the aforementioned recombination mechanisms, identified through the comparison of linear and circular TR measurements. The same sets of measurements for thinner films (4.4 nm $\leq d <$ 20 nm) revealed an additional relaxation dynamic ($\tau \sim 10$ ps), which is attributed to the enhanced surface recombination of charge carriers. Our DFT+U calculations further corroborate this observation, indicating an increase in the surface density of states with decreasing film thickness which results in higher amplitude and smaller time constant for surface recombination as the film thickness decreases.

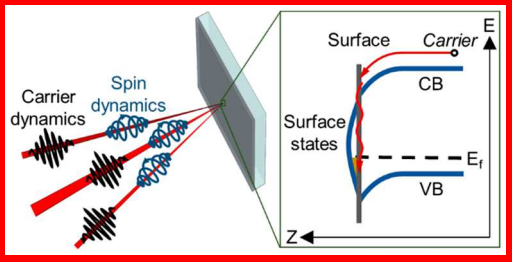

surface recombination, pump−probe spectroscopy, perovskite oxide $La_{0.7}Sr_{0.3}MnO_3$ thin film, DFT+U, spin polarization

Perovskite oxide $La_{0.7}Sr_{0.3}MnO_3$ (LSMO) [Figure 1] is a strongly correlated half-metal exhibiting colossal magnetoresistance,[1−3] a Curie temperature above room temperature ($T_c \cong 370$ K),[4] magnetic properties that depends on oxygen vacancy, film thickness, strain, *etc.*[5−7] Consequently this material has been proposed for applications in magnetic tunnel junctions and solid oxide fuel cells.[8−10] Moreover, this strongly correlated system has distinct physical properties that can be tuned by changing the growth conditions, such as thickness, substrate, doping level, oxygen defect concentration, and deposition conditions.[5,11,12] The tunability of physical properties enables one to change the band structure, the dopant level and occupancy, resulting in a material that has the potential for light harvesting, magneto-optic, and optoelectronic devices.[13,14]

Previous studies on bulk LSMO films have identified electron−phonon relaxation ($\tau < 1$ ps) and phonon-assisted spin−lattice relaxation ($\tau \sim 10$ ps) through the low-temperature-dependent transient-optical response.[15−17] However, there is limited information about this response in thin films near room temperature, which will be relevant for many future device applications and where differences in ultrafast dynamics due to surface and interface effects are expected. For

Received: December 19, 2018
Accepted: February 26, 2019
Published: February 26, 2019

Downloaded via WEST VIRGINIA UNIV on August 27, 2019 at 22:17:02 (UTC).
See https://pubs.acs.org/sharingguidelines for options on how to legitimately share published articles.

© 2019 American Chemical Society

DOI: 10.1021/acsnano.8b09595
ACS Nano 2019, 13, 3457−3465

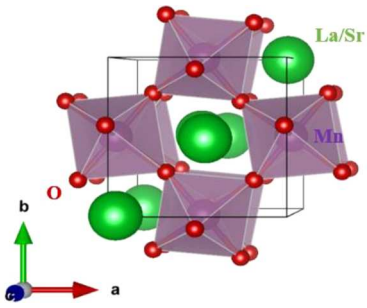

Figure 1. Crystal structure of LSMO.

example, by decreasing the film thickness, the surface to bulk ratio increases and the surface electrons dominate the features from the bulk electrons. Subsequently, additional energy states (midgap surface states or Tamm levels) emerge between the valence band and the conduction band extrema, providing extra relaxation channels.[18] A thorough study of the surface states is critical for a device application point of view because recombination due to these states drastically affects the efficiency of optoelectronic devices.[19,20] Moreover, surface effects can oxidize the sample and form defects that can reduce the longevity of the device.[21,22]

In the present work, we perform a thickness dependence study of the photocarrier and associated spin dynamics in LSMO thin films, determined by TR measurements with subpicosecond time resolution at room temperature. Variation of the thickness provides insight into changes in the physical properties from LSMO bulk crystals, with a particular focus on effects arising from the additional surface states. For comparison, first-principles calculations and TR experiments on the thicker LSMO films (bulk) reveal large spin-polarity in the optical transitions, occurring through $O(2p) \rightarrow Mn(3d)$ transition. While our results on the bulk LSMO films are consistent with previous reports,[15−17] excitation-density dependent TR on thinner LSMO films (d < 20 nm) reveals a faster relaxation mechanism ($\tau \sim 10$ ps), which is attributed to the surface recombination. DFT calculations also indicate a significant enhancement in the surface density of states (DOS) with decreasing film thickness, yielding an additional surface relaxation mechanism in ultrathin films.

RESULTS AND DISCUSSION

Figure 2a shows the effect of different excitation fluences, and consequently an increasing number of free carriers, on the free carrier dynamics of 43.1 nm LSMO on top of the STO substrate. The dynamics start with a negative rise in the TR signal as the electrons excite to higher energy states, followed by a decaying signal. This transient can be analyzed phenomenologically by fitting a product of a multiexponential decay and a Gaussian error function to the data, as follows:[23]

$$\frac{\Delta R}{R} = \sum_{i=1}^{n} \frac{1}{2} A_i \left[1 + \mathrm{erf}\left(\frac{t}{\tau_r}\right)\right] \times \exp\left(\frac{-t}{\tau_{d_i}}\right) \quad (1)$$

Here, n, τ_r, A, and τ_d are the number of decay components, rise time constant, amplitude, and decay time constant of each component, respectively. Care was taken to minimize the number of decays while getting an acceptable fit, to avoid overfitting.

For the 43.1 nm film, the fitting results show one negative rise and three decay components for all the excitation fluences (fit parameters are listed in the Supporting Information Table 1). Because the pump photon energy is higher than the energy needed for some optical transitions in half-conducting LSMO[1,24] [Figure 3e] and lower than the optical bandgap of the substrate (STO), the pump pulse will excite the electron−hole pairs above the bandgap of the film but not of the

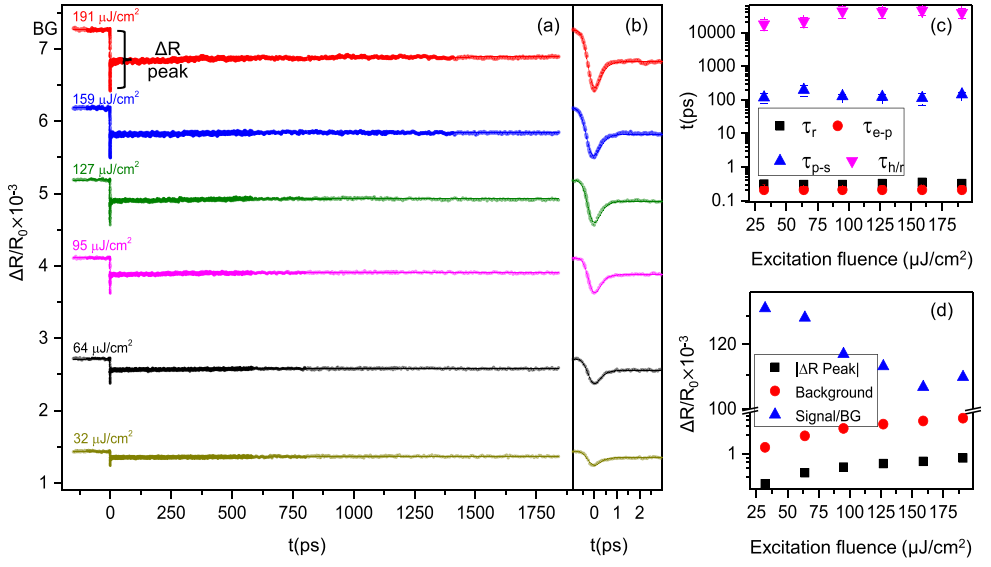

Figure 2. (a) TR measurements for 43.1 nm LSMO thin film on STO substrate with different excitation fluences. (b) TR measurements zoomed in to the first 3 ps to show the ultrafast decay due to the electron−phonon interaction. (c) Decay time constants for different decay components as a function of excitation fluence. $\tau_{h/r}$ increases with pump fluence, while τ_{e-p}, τ_{p-s}, and τ_r are almost independent of the excitation fluence. (d) The absolute value of $\Delta R/R_0$ and background plateau as a function of excitation fluence. While both background and the peak increase by the fluence, the large difference between the background and peak shows the hindrance in the signal acquisition. The background is due to coherent effect from scattered pump pulses and/or a very slow relaxation mechanism which takes longer than 12.5 ns when the next pulse excites the electrons again.

DOI: 10.1021/acsnano.8b09595
ACS Nano 2019, 13, 3457−3465

substrate. The possible excitations shown in Figure 3e result in an absorption decrease due to Pauli blockings as the conduction states fill up, causing the refractive index to decrease, based on Kramers−Kronig integrals. The decrease in the refractive index will result in a negative $\Delta R/R_0$ signal at $t = 0$.[13,25] This process happens in a subpicosecond scale[26−28] and corresponds to a fitted rise time (τ_r) of ∼0.3 ps, which is independent of the excitation fluence.

Figure 2c provides more insight into the fit results of TR measurements for 43.1 nm LSMO film. After the negative rise, the electrons (which are now in the conduction band) will couple with the phonons and relax back to the bottom of the conduction band in a subpicosecond time scale.[29] The ultrafast decay time constant (τ_{e-p}) of ∼0.2 ps is also independent of pump fluence and is consistent with electron−phonon relaxation in LSMO and other similar systems.[15,16,26,27] The medium time constant (τ_{p-s}) which is on the order of tens of picoseconds and has previously been proven to be due to phonon-assisted spin−lattice relaxation,[15,16,29,30] is almost independent of the excitation fluence. The slow time constant ($\tau_{h/r}$), which is on the order of nanoseconds and is beyond the measurement range of the setup, indicates an increase with increasing the laser fluence. The relaxation phenomena in this time scale could either be due to heat diffusion or slow radiative recombination.[29] In the first case, there will be a large positive offset at long time delays (compared to the background signal) in the $\Delta R/R_0$ signal because all the absorbed energy will heat up the lattice.[16,27] However, for the latter case, only the extra energy after releasing energy (as large as the bandgap) radiatively, will transfer to the lattice as heating, and this will cause a negative or a small positive offset in the accessible time scale.[27] As one can see in the case of our study, the offset at long time delays is negative, which indicates radiative recombination. On the other hand, the large background shown in Figure 2d, which means the electrons cannot release all their energy before the next pulse excites them again (12.5 ns), indicates a slow thermal diffusion in the sample. The data presented here is consistent with the data presented in ref 16 at low temperatures.

As Bennett *et al.*[25] explained, due to the large effective hole masses, which leads to higher electronic DOS, the band filling effect in p-doped systems is not strong, resulting in smaller ΔR peaks. Parlato *et al.*[16] mentioned that at temperatures above 130 K, the signal-to-noise ratio of the LSMO thin film TR signal significantly decreases and to get a less noisy signal one should increase the excitation intensity. However, higher excitation intensity results in sample heating and destruction. As the reference indicated,[16] a large positive plateau in the signal, which is due to the heated or destroyed sample, alters the material's carrier dynamics. This hindrance was overcome by averaging high numbers of scans to reduce the noise statistically. This method enabled us to extract the dynamics even in the presence of considerable noise. The minimum considered number of scans to perform this analysis was 25 for the thickest film and for the highest excitation intensity, while it was 50 for thin samples. The signal-to-noise ratio presented here is comparable to the one reported in ref 16 at low temperature. The background magnitude increases linearly with the pump fluence. The peak magnitude in the signal also monotonically increases with the pump fluence. However, this increase is not as strong as the increase in the background due to the excitation fluence. This difference in the slopes makes the signal for lower pump fluences less noisy [Figure 2d].

The half-metallicity of the films results in having a much stronger transient signal for one spin channel and a very weak transient signal for the other spin channel, at zero Kelvin. It is expected that by increasing the temperature, the half-metallicity of the system decreases. Performing spin dynamic measurements using a similar pump−probe setup with circularly polarized light proves the significant half-metallicity of the system if electrons are excited only for one spin component. Figure 3a represents spin dynamic measurements for different excitation powers. As expected for half-metallic thin films at room temperature, the excitation is stronger for one of the spin components (in this case $\text{pump}_{LCP} - \text{probe}_{RCP}$) compare to the other one ($\text{pump}_{LCP} - \text{probe}_{LCP}$). The inset of Figure 3a indicates the time-resolved degree of spin polarization, calculated from $P = \frac{I_R - I_L}{I_R + I_L}$, for different excitation powers. Because spins of the electrons are polarized by the exciting light, a more intense pump beam can polarize more spins. Hence, as expected, by increasing the excitation power, the degree of spin polarization increases.[31] Because for this component we observe the same dynamics as the carrier dynamics from the linear polarization configuration, one can relate all the dynamics in LSMO half-metallic thin films to the spin systems.[32,33] As can be seen in Figure 5b and Supporting Information, Figure 3, the contribution of the electron−phonon interactions in LSMO free carrier dynamics is the strongest contribution. These elastic scatterings play an important role in spin relaxation in higher temperatures.[34] Figure 3a shows stronger subpicosecond recombination for higher excitation powers. This subpicosecond recombination has been attributed to electron−phonon interactions in Figure 2 of the main text and Figure 3 of the Supporting Information, indicating that by increasing the temperature (excitation intensity), the intensity of spin relaxation due to electron−phonon interactions increases. Moreover, the inset of Figure 3a indicates a sharp drop in the degree of spin polarization in the same time regime as the electron−phonon interactions. Hence this subpicosecond drop in the spin polarization is attributed to the electron−phonon interactions.

Figure 3b shows the distribution of the net spin-moments (*i.e.*, majority−minority spins) in the bulk LSMO crystal. An ample portion of the net spin-moment is concentrated at Mn sites. The PBEsol+U predicted magnetic moment is 3.5 μ_B per Mn atom, which is in good agreement with the experimental value of 3.7 ± 0.1 μ_B per Mn.[36] Oxygen atoms also acquire a small but nonzero magnetic moment, as shown in Figure 3b, due to the strong hybridization of O-2*p* orbitals with Mn-3*d* states as well as due to the double exchange mechanism. The absolute value of the average magnetic moment per oxygen atom is ∼0.03 μ_B, which is consistent with previous reports.[37] Figure 3d,e represents the orbital projected electronic band structure of LSMO for minority and majority spin-channels, calculated along the high symmetry directions of the BZ shown in Figure 3c. The projection of minority spins on the electronic bands reveals the insulating feature for the minority spin-channel with an energy gap of ∼2.85 eV, whereas metallic features can be observed for the majority spin-channel. The shaded area in Figure 3d,e depicts the energy window of 1.53 ± 0.01 eV below the Fermi level, marking the region from where the pump pulse (810 nm) used in our TR measurements could potentially excite the charge carriers to the unoccupied states. For the minority spin-channel, the possible transitions could occur only from the occupied O (2*p*) states

DOI: 10.1021/acsnano.8b09595
ACS Nano 2019, 13, 3457−3465

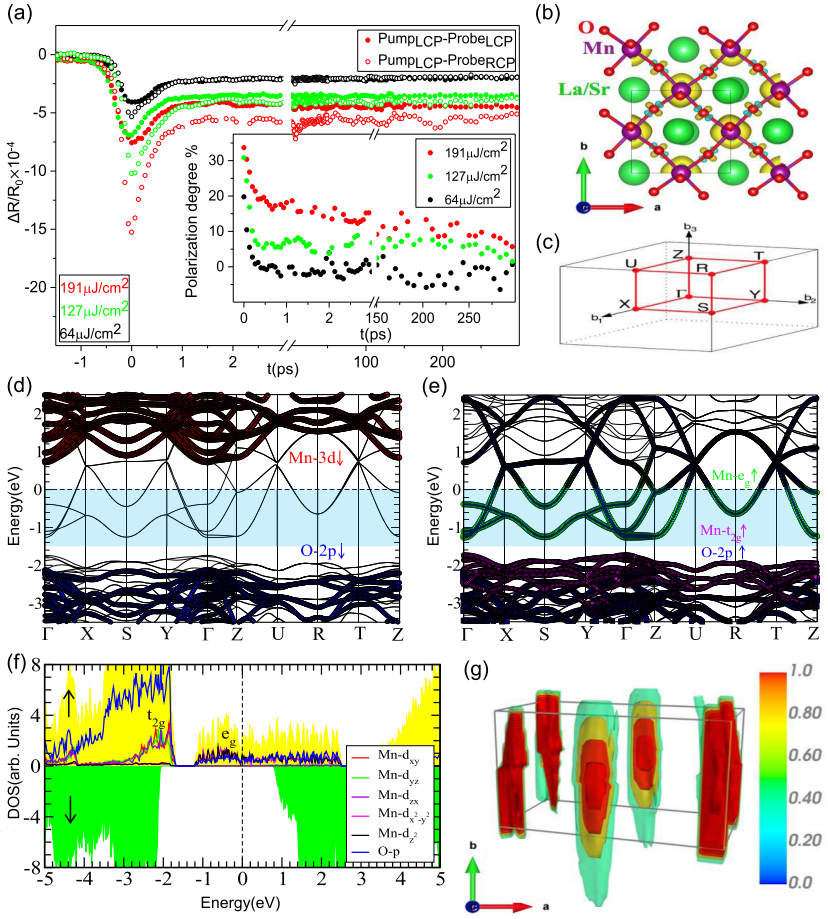

Figure 3. (a) Spin dynamic measurements for different excitation powers at room temperature. The inset indicates an increase in the degree of spin polarization by increasing the excitation intensity. (b) Crystal structure of LSMO projected with the net spin-moment (= majority − minority spins) at an isosurface value of 0.01. (c) BZ of LSMO obtained using AFLOW software.[35] Orbitals projected electronic band structure for (d) minority spin-channel and (e) majority spin-channel. The shaded areas depict the energy window of 1.53 ± 0.01 eV, which is the range of the excitation energy of the used laser pump pulse. (f) Orbitals projected DOS for bulk LSMO. Yellow/green color highlights the total DOS for majority/minority spin-channels. (g) An isosurface representation of the normalized square of the optical dipole transition matrix element in the irreducible BZ for majority spin states.

to the empty Mn ($3d$) states. However, these transitions cannot occur in our experiments because the used photon energy is smaller than the optical bandgap of the minority spin channel.

For the majority spin-channel, there are several occupied states available for the pump excitation [Figure 3e]. These occupied majority spin-states are mainly composed of O ($2p$) and Mn (t_{2g}) states. The atomic orbitals resolved DOS plot [Figure 3f] for the majority channel clearly indicate that occupied Mn ($d_{xy,\ yz,\ zx}$) and O ($2p$) states constitute valence bands below the energy bandgap region, whereas Mn ($d_{x^2-y^2}, d_{z^2}$) orbitals together with O ($2p$) orbitals form the valence and conduction band states dispersed near the Fermi level. In the shaded energy window, O ($2p$) orbitals highly overlap with Mn (e_g) states. Therefore, maximum optical transitions from occupied to empty states are expected to occur among the O ($2p$) and Mn (e_g) states. No optical transition is expected to occur from the Mn (t_{2g}) states by means of the laser pump used in this study.

To determine the magnitude of the optical transitions at different points of the BZ, we analyze the dipole transition matrix elements ($\mathcal{M}$) calculated using the method described in the ref 38. Because the majority spin-states near Fermi-level are highly intermixed, we evaluate the average $\mathcal{M}^2$ for different possible interband optical transitions between two states (one occupied and one unoccupied) corresponding to $\Delta E = 1.53 \pm 0.01$ eV, where ΔE is the difference in the energy of the *final* unoccupied and *initial* occupied state. This energy is equivalent to the excitation energy of the laser pump. An isosurface representation of the normalized $\mathcal{M}^2$ for majority spin-channels is shown in Figure 3g. As expected from the electronic band structure calculations and observed in our TR measurements for different polarizations of the laser beam, we notice a strong optical excitation for the majority spin-channel. The major optical transitions occur near the high-symmetry points and along the high-symmetry lines of the BZ.

Figure 4 shows the TR measurements results after normalizing the background on LSMO samples with different thicknesses. While films with thickness above ∼20 nm have the same type of dynamics, thinner films show an extra relaxation mechanism emerging as the LSMO film becomes thinner (fit parameters are given in the Supporting Information, Tables 2 and 3). TR measurements were performed on LSMO thin films of various thicknesses, with the excitation and probe fluence of 191 and 3 μJ/cm^2, respectively. For 43.1 and 20.3 nm thin films, the fit was converged with three decay

DOI: 10.1021/acsnano.8b09595
ACS Nano 2019, 13, 3457−3465

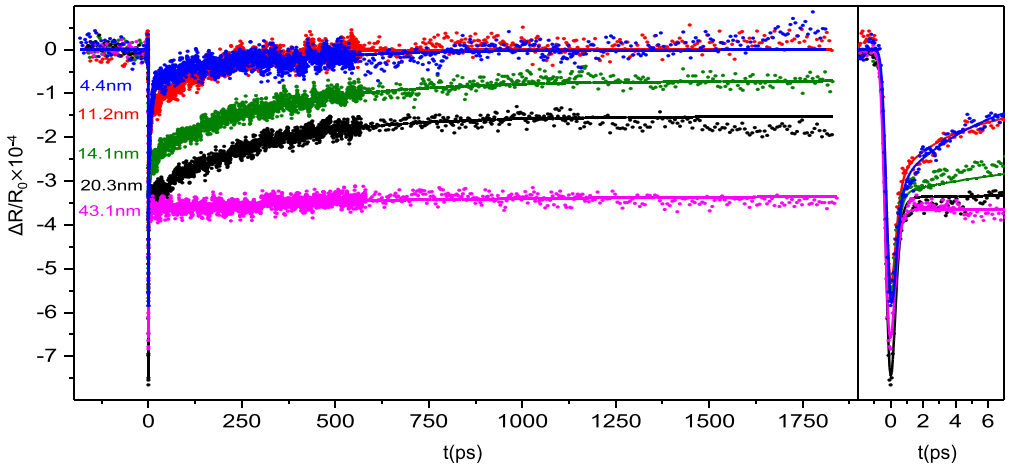

Figure 4. TR measurements for LSMO thin films with different thicknesses. For thinner films, an extra relaxation mechanism was observed. For the 14.1 nm film, all four dynamics were observed, however, thinner films lose all their energy after hundreds of picoseconds and no loss of energy due to heat diffusion or radiative recombination was observed.

components in ranges of subpicosecond, tens, and thousands of picoseconds. However, for films thinner than 11.2 nm, the range of the three decay components, which gave the best fit results, were subpicosecond, a few, and hundreds of picoseconds. For 14.1 nm LSMO thin film three decay components model failed to fit the data. Adding an extra decay component solved this problem and resulted in four decay components in the range of subpicosecond (τ_{e-p}), a few (τ_s), tens (τ_{p-s}) and thousands of picoseconds ($\tau_{h/r}$). Having an extra mechanism emerging as the surface electrons start to dominate the bulk electrons, to study the emergence of the additional phenomena, a different version of the fit, with four decay components, was performed for all the data to be thorough regardless of signs of overfitting (*i.e.* very small amplitudes, the same decay time constant, *etc*). As a result of overfitting for some of the films, larger error bars have appeared [Figure 5a,b], and the fit with the optimum number of decay components with acceptable error bars are presented in the Supporting Information (Figure 4).

As the result of fitting with four decay components, Figure 5a,b show the decay time constant and amplitude of each decay component. While τ_r, τ_{e-p} and τ_{p-s}, are almost independent of the film thickness, τ_s and $\tau_{h/r}$ increase with the film thickness. The amplitude plot [Figure 5b] shows the electrons lose most of their energy via interaction with phonons, because the magnitude of the amplitudes for the electron−phonon decay components (red) are almost an order of magnitude higher than the other components. The other three decay components almost have the same contribution to the electrons' energy relaxation. By decreasing the film thickness, the quantum confinement becomes a matter of great importance. The general increase in the electron−phonon relaxation amplitude with thickness shows that the bandgap decreases with thickness and the interaction with phonons become less effective in larger bandgaps (thinner films), which is consistent with quantum size effect for strongly correlated LSMO half-metal system.[39,40] Figure 5a indicates a separate mechanism (τ_s) as the film thickness decreases, however, this mechanism becomes indistinguishable from the phonon-assisted spin−lattice recombination as the film thickness reaches its bulk value. We attribute this separate mechanism to surface recombination because it happens when the surface to bulk ratio increases. Moreover, as discussed in the ref 18, because the lattice mismatch between the substrate and the film is small,[41] unwarranted interface traps are negligible. The decrease of the surface recombination time constant (τ_s) by decreasing the thickness indicates the path length for an electron to reach the surface to recombine with the surface states reduces, resulting in a faster recombination time constant in thinner films. Figure 5b shows the strong effect of surface recombination in thinner films (less than ∼20 nm thick), and in these films, electrons lose most of their energy without any radiative or thermal recombination. On the other hand, as the thickness increases, because the bulk carrier density dominates the surface carrier density, the surface recombination appears to be negligible with respect to the other decay components. In the thicker films (above ∼20 nm thick), strong radiative or thermal recombination are responsible for the energy loss in the electrons.

Figure 5c represents the calculated surface DOS for 4 and 8 unit cells LSMO thin films mounted on a 5 unit cells STO substrate. In the same figure, we also present the DOS for bulk LSMO for comparison. We notice an increase in the DOS near the Fermi level as the thickness decreases, thus indicating a higher density of surface states in thinner films. Figure 5d shows the integrated DOS in the energy window of [−0.25, 0.25] eV, further suggesting a systematic increase in the surface DOS in thinner films close to the Fermi energy. Having a higher density of surface states results in higher transition probability through surface states and consequently a higher amplitude for the surface recombination in thinner films, which is consistent with the fit results in Figure 5b. Moreover, the averaged electric potential ($\frac{\partial V_z}{\partial z}$) along the vertical direction rapidly increases with decreasing thickness of deposited LSMO films, as reported by Trappen *et al.* in a recent work.[41] This causes an increase in the electric field along a direction perpendicular to the LSMO surface, leading to more energy band bending near the surface[42,43] and consequently a faster surface recombination of charges in thinner films, which is consistent with the fitting results presented in Figure 5a.

Figure 6 shows TR measurements for different excitation fluences for 4.4 nm LSMO thin film with the focus on the surface recombination. The inset of Figure 6 indicates the dependence of the decay lifetime of the surface relaxation

DOI: 10.1021/acsnano.8b09595
ACS Nano 2019, 13, 3457−3465

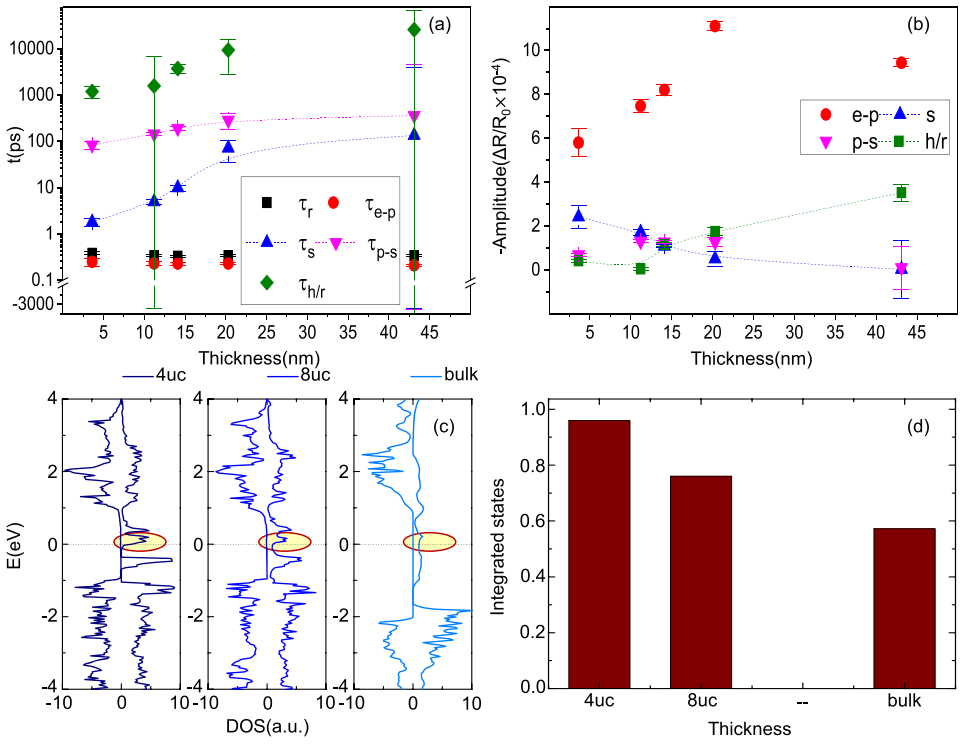

Figure 5. (a) Decay time constants for different films showing the surface recombination time constant (blue dots) increases with the thickness. (b) Negative amplitudes of decay components showing the energy dissipated by the surface recombination decay component is comparable to the lost energy due to phonon-assisted spin-lattice recombination and heat diffusion/radiative recombination. The surface recombination becomes stronger as the films become thinner. (c) DOS for 4 and 8 unit cells LSMO thin films compared to bulk LSMO, indicating the density of surface states increase by decreasing the film thickness. (d) integrated DOS in the energy window of [−0.25, 0.25] eV.

mechanism with pump fluence for the 4.4 nm LSMO thin film. There is a linear decrease in the decay lifetime with increasing excitation fluence. This decrease can be qualitatively understood by utilizing the relations among excitation power, temperature, and the kinetic energy of charge carriers. According to Lin,[44] the maximum pulsed laser temperature varies almost quadratically with the laser power (P), *i.e.* $T \propto P^2$. The kinetic energy of carriers of effective mass m and velocity v can be expressed as

$$\frac{1}{2}mv^2 \equiv \frac{3}{2}k_B T \propto P^2 \tag{2}$$

where, k_B is the Boltzmann constant. From the above expression, one notices that v is linearly proportional to the laser power P. Therefore, the higher the laser power, the higher the surface recombination velocity and thus shorter time ($t \sim 1/v$) for recombination.[18] This decrease in the surface recombination time constant is consistent with the surface recombination velocity because by increasing the thin film temperature (due to the laser power increase), surface recombination velocity increases. Consequently electrons on the surface recombine faster,[18] suggesting ultrathin LSMO films as a suitable material for the future ultrafast optoelectronic and magneto-optic devices.

CONCLUSION

Surface recombination at room temperature in complex oxide LSMO ultrathin films which can significantly affect device applications has been studied in this work. The TR measurement at room temperature for films above ∼20 nm

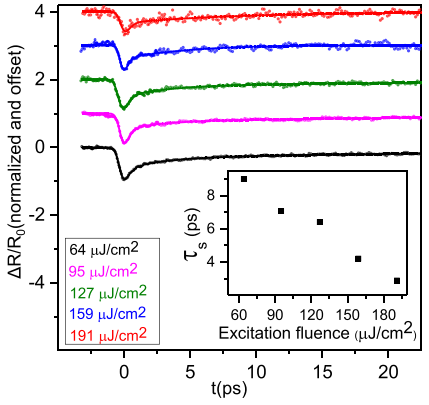

Figure 6. TR signal excitation fluence dependence for 4.4 nm LSMO thin film shows that the surface recombination decay time constant decreases with laser fluence.

thick, is consistent with results already published in the literature at lower temperatures. These measurements indicate three relaxation mechanisms. (i) Electron−phonon recombination (τ < 1 ps), (ii) phonon-assisted spin−lattice recombination ($\tau \sim$ 100 ps), and (iii) thermal diffusion/radiative recombination (τ > 1 ns). Circular TR measurements indicate that due to LSMO's half-metallic behavior, the dominant carrier dynamics come from the conducting spin majority channel, while almost no response is observed from the insulating spin minority channel. DFT calculations enabled us to determine the possible transitions and their probabilities responsible for the recombination, indicating major optical

DOI: 10.1021/acsnano.8b09595
ACS Nano 2019, 13, 3457−3465

transitions occurring in the majority spin-channel and near the high-symmetry points, S, T, Γ, and R, of the BZ. Reducing the film thickness, enabled the study of the surface effect on LSMO thin films as the surface contribution increases with respect to the bulk contribution in thinner films. Consistent with the experimental observation of surface recombination for films thinner than ∼20 nm, DFT calculations indicate an increase in the density of the surface states in thinner films, which consequently results in stronger surface recombination. Reduction in the path length from the bulk to the surface and increase in the energy band bending near the surface, result in faster surface recombination in thinner films. Moreover, the surface decay time constant monotonically decreases with increasing excitation fluence, indicating higher carrier velocity for higher excitation fluences.

METHOD AND EXPERIMENTAL

Sample Preparation. Perovskite oxide LSMO thin films were fabricated with different thicknesses by pulsed laser deposition (PLD) on (100) $SrTiO_3$ single crystal substrates. The target material is ablated using a KrF laser at a wavelength of 248 nm with an energy fluence of 300 mJ/pulse. Before growing the sample, the substrates were annealed to form terraces to encourage layer-by-layer growth. All of the samples were grown under the same optimized conditions of 750 °C and 100 mTorr oxygen pressure, optimized by *in situ* reflection high energy electron diffraction (RHEED). After growth, the samples were postannealed in oxygen at 250 mTorr to minimize the presence of oxygen vacancies. The quality of the thin films was checked with X-ray diffraction (XRD), vibrating sample magnetometry (VSM), and atomic force microscopy (AFM). Materials characterization results for one of the films as an example are shown in the Supporting Information (Figures 1 and 2), and more information can be found in ref 45. The films thicknesses were confirmed by X-ray reflectivity (XRR) to be 4.4, 11.2, 14.1, 20.3, and 43.1 nm.

Optical Measurements. Figure 7 provides a simplified schematic diagram of the TR geometries used in this paper for both circular and

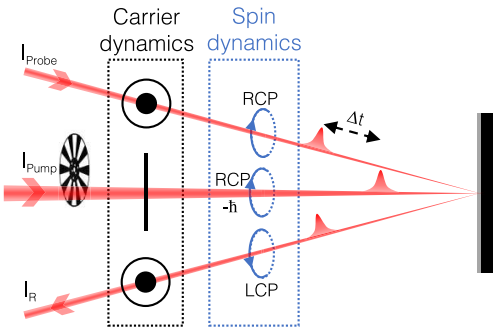

Figure 7. Schematic diagram of the measurements.

linear polarization configurations. TR was performed with a degenerate pump−probe setup using a Spectra-Physics Tsunami Ti:sapphire laser source at 810 nm (photon energy of 1.53 ev) with a repetition rate of 80 MHz and nominal pulse duration of 100 fs. The pump pulse was normal to the sample, while the probe had an incident angle of 15°. Pump pulses were modulated by a mechanical chopper at a reference frequency of 3 kHz and were focused to a $\frac{1}{e^2}$ spot diameter of 50 μm, twice the size of the probe spot diameter. A range of pump excitation densities with fluences of 32−191 $\mu J/cm^2$ were used in the experiments, meanwhile, the fluence of the probe pulse was kept constant at 3 $\mu J/cm^2$. Detection of the optical signal was recorded in a lock-in amplifier locked to the reference frequency. Transients were measured by varying a mechanical delay stage that has a range of 1.8 ns with a precision of 66 fs. For linear-polarized configuration, the pump and probe pulses were cross linearly polarized to minimize pump scatter and coherent effects caused by the direct interference of the two pulses at zero delay time.

A circular pump−probe experiment has been performed to study the spin polarization of the system and spin dependent dynamics. For circular measurements, additional zero-order achromatic quartz-MgF_2 quarter waveplates with a performing wavelength range of 700−1000 nm were introduced to perform co- and cross-circular measurements. After reflection, a quarter waveplate was used to change the polarization of the circularly polarized probe to linearly polarized light, which passes through a linear analyzer and reaches the detector. In this setup, a right (left) circular polarized pump beam, RCP (LCP), changes the *J*-state of the electrons by $-\hbar$ ($+\hbar$) and the circularly polarized probe beam traces the m_j states.[32,46] Because bulk LSMO is a half-metallic ferromagnet with more than 90% spin polarization, almost no minority charge carriers are at the Fermi level at absolute zero temperature.[46]

DFT Calculations. To understand the origin and nature of the optical transitions in bulk LSMO, we performed first-principles DFT +U calculations using VASP code (version 5.3.3).[38,47,48] The generalized gradient approximation (GGA) for solids as parametrized by Perdew−Becke−Ernzerhof (PBEsol) was used for the exchange-correlation (XC) functional.[49] The projected augmented wave (PAW) method[50,51] with a kinetic energy cutoff of 600 eV for the plane wave basis set was employed. We considered 11 valence electrons of La ($5s^25p^65d^16s^2$, version 06Sep2000), 10 valence electrons of Sr ($4s^24p^65s^2$, version 07Sep2000), 13 valence electrons of Mn ($3p^64s^23d^5$, version 02Aug2007), 12 valence electrons of Ti ($3s^23p^63d^24s^2$, version 26Sep2005), and 6 valence electrons of O ($2s^22p^4$, version 08Apr2002) in the PAW pseudopotentials. La/Sr concentration ratio of 0.70/0.30 was simulated using the virtual crystal approximation (VCA).[52] A 9 × 9 × 6 Monkhorst−Pack *k*-point mesh[53] was used for the structural optimization, and a 18 × 18 × 12 Monkhorst−Pack *k*-point mesh was used to calculate the optical transition matrix elements.[38] To correctly evaluate the strong-correlation effects in LSMO, we employed rotationally invariant DFT+U method[54] with U = 2.7 eV and J = 1.0 eV, after testing various other combinations of U and J values. Our calculations suggest that the aforementioned U and J values correctly predict the half-metallicity and the ferromagnetic (FM) ground state of bulk LSMO. Previous studies have also used this combination of U and J values to correctly reproduce the experimental observations.[41,55] The PBEsol +U predicted Mn−O bond length is 1.95 Å, which is in excellent agreement with the reported experimental value of 1.95 Å.[56,57] The optimized lattice parameters for bulk unit cell are a = 5.445 Å, b = 5.461 Å, and c = 7.675 Å, which are consistent with the reported values in literature.[56] Having the electronic band structure and optical transition probabilities for different spin channels obtained using DFT calculations, one can relate the results of the TR measurements (electrons relaxation mechanisms) to specific optical transitions for different spin channels and points in the Brillouin zone (BZ).

To study the thickness dependence of surface states in LSMO thin films mounted on STO substrate, we prepared two slabs consisting of five cubic layers of STO and added four and eight layers of LSMO on top of the STO substrate. We added an extra layer of oxygen atoms to complete the Mn−O octahedral at the LSMO surface. A vacuum of thickness 16 Å was added perpendicular to the LSMO surface to avoid any interaction in the periodic geometries. During the structural optimization, the lowest STO layer was frozen to simulate the bulk substrate behavior, whereas all other atoms were allowed to freely relax until the net residual force on each atom was less than 0.001 eV/Å. An 8 × 8 × 1 Monkhorst−Pack *k*-mesh was used to sample the reciprocal space of LSMO/STO slabs.

ASSOCIATED CONTENT

Supporting Information

The Supporting Information is available free of charge on the ACS Publications website at DOI: 10.1021/acsnano.8b09595.

DOI: 10.1021/acsnano.8b09595
ACS Nano 2019, 13, 3457−3465

Thin films characterization and more discussion on the fit parameters (DOCX)

AUTHOR INFORMATION

Corresponding Authors

*E-mail: mikel.holcomb@mail.wvu.edu.
*E-mail: Aldo.Romero@mail.wvu.edu.

ORCID

Saeed Yousefi Sarraf: 0000-0003-2972-4654
Sobhit Singh: 0000-0002-5292-4235
Robbyn Trappen: 0000-0002-2676-483X

Notes

The authors declare no competing financial interest.

ACKNOWLEDGMENTS

We acknowledge American Chemical Society for student support (PRF 56642-ND10), National Science Foundation for thin film growth and optimization (DMR-1608656), and U.S. Department of Energy for optics supplies and theory contributions (DE-SC0016176). This work used the XSEDE, which is supported by National Science Foundation under grant number ACI-1053575. We acknowledge the support from the Texas Advances Computer Center with the Stampede and Bridges supercomputers. A.H.R., S.S., and A.C.G. also acknowledge the support of DMREF-NSF 1434897 and NSF OAC-1740111.

REFERENCES

(1) Haghiri-Gosnet, A.-M.; Renard, J.-P. CMR Manganites: Physics, Thin Films and Devices. *J. Phys. D: Appl. Phys.* **2003**, *36*, R127.

(2) Veis, M.; Višňovský, Š.; Lecoeur, P.; Haghiri-Gosnet, A.-M.; Renard, J.-P.; Beauvillain, P.; Prellier, W.; Mercey, B.; Mistrík, J.; Yamaguchi, T. Magneto-Optic Spectroscopy of $La_{2/3}Sr_{1/3}MnO_3$ Films on $SrTiO_3$ (1 0 0) and (1 1 0) Substrates. *J. Phys. D: Appl. Phys.* **2009**, *42*, 195002.

(3) Damjanovic, D. Ferroelectric, Dielectric and Piezoelectric Properties of Ferroelectric Thin Films and Ceramics. *Rep. Prog. Phys.* **1998**, *61*, 1267−1324.

(4) Jonker, G. H.; Van Santen, J. H. Ferromagnetic Compounds of Manganese with Perovskite Structure. *Physica* **1950**, *16*, 337−349.

(5) Pradhan, A. K.; Hunter, D.; Williams, T.; Lasley-Hunter, B.; Bah, R.; Mustafa, H.; Rakhimov, R.; Zhang, J.; Sellmyer, D. J.; Carpenter, E. E.; Sahu, D. R.; Huang, J.-L. Magnetic Properties of $La_{0.6}Sr_{0.4}MnO_3$ Thin Films on $SrTiO_3$ and Buffered Si Substrates with Varying Thickness. *J. Appl. Phys.* **2008**, *103*, No. 023914.

(6) Haghiri-Gosnet, A. M.; Wolfman, J.; Mercey, B.; Simon, C.; Lecoeur, P.; Korzenski, M.; Hervieu, M.; Desfeux, R.; Baldinozzi, G. Microstructure and Magnetic Properties of Strained $La_{0.7}Sr_{0.3}MnO_3$ Thin Films. *J. Appl. Phys.* **2000**, *88*, 4257−4264.

(7) Guo, E.-J.; Charlton, T.; Ambaye, H.; Desautels, R. D.; Lee, H. N.; Fitzsimmons, M. R. Orientation Control of Interfacial Magnetism at $La_{0.67}Sr_{0.33}MnO_3$ /$SrTiO_3$ Interfaces. *ACS Appl. Mater. Interfaces* **2017**, *9*, 19307−19312.

(8) Solignac, A.; Guerrero, R.; Agnus, G.; Fermon, C.; Pannetier-Lecoeur, M.; Lecoeur, P. Magnetic Tunnels Junctions for All-Oxide Spin Valves Devices. *J. Phys.: Conf. Ser.* **2011**, *303*, No. 012059.

(9) Moreno, C.; Munuera, C.; Valencia, S.; Kronast, F.; Obradors, X.; Ocal, C. Reversible Resistive Switching and Multilevel Recording in $La_{0.7}Sr_{0.3}MnO_3$ Thin Films for Low Cost Nonvolatile Memories. *Nano Lett.* **2010**, *10*, 3828−3835.

(10) Alldredge, L. M. B.; Chopdekar, R. V.; Nelson-Cheeseman, B. B.; Suzuki, Y. Spin-Polarized Conduction in Oxide Magnetic Tunnel Junctions with Magnetic and Nonmagnetic Insulating Barrier Layers. *Appl. Phys. Lett.* **2006**, *89*, 182504.

(11) Yang, F.; Kemik, N.; Biegalski, M. D.; Christen, H. M.; Arenholz, E.; Takamura, Y. Strain Engineering to Control the Magnetic and Magnetotransport Properties of $La_{0.67}Sr_{0.33}MnO_3$ Thin Films. *Appl. Phys. Lett.* **2010**, *97*, No. 092503.

(12) Majumdar, S.; van Dijken, S. Pulsed Laser Deposition of $La_{1-x}Sr_xMnO_3$: Thin-Film Properties and Spintronic Applications. *J. Phys. D: Appl. Phys.* **2014**, *47*, No. 034010.

(13) Smolin, S. Y.; Scafetta, M. D.; Guglietta, G. W.; Baxter, J. B.; May, S. J. Ultrafast Transient Reflectance of Epitaxial Semiconducting Perovskite Thin Films. *Appl. Phys. Lett.* **2014**, *105*, No. 022103.

(14) Smolin, S. Y.; Scafetta, M. D.; Choquette, A. K.; Sfeir, M. Y.; Baxter, J. B.; May, S. J. Static and Dynamic Optical Properties of $La_{1-X}Sr_xFeO_{3-\delta}$: The Effects of A-Site and Oxygen Stoichiometry. *Chem. Mater.* **2016**, *28*, 97−105.

(15) Lobad, A. I.; Averitt, R. D.; Kwon, C.; Taylor, A. J. Spin−Lattice Interaction in Colossal Magnetoresistance Manganites. *Appl. Phys. Lett.* **2000**, *77*, 4025−4027.

(16) Parlato, L.; Arpaia, R.; De Lisio, C.; Miletto Granozio, F.; Pepe, G. P.; Perna, P.; Pagliarulo, V.; Bonavolontà, C.; Radovic, M.; Wang, Y.; Sobolewski, R.; Scotti di Uccio, U. Time-Resolved Optical Response of All-Oxide $YBa_2Cu_3O_7/La_{0.7}Sr_{0.3}MnO_3$ Proximitized Bilayers. *Phys. Rev. B: Condens. Matter Mater. Phys.* **2013**, *87*, 134514.

(17) Peng, L.; Cai, C.; Xu, D. H.; Liu, Y. Ultrafast Optical Probes of Dynamic Behavior in $La_{0.7}Sr_{0.3}MnO_3/YBa_2Cu_3O_{7-\delta}/La_{0.7}Sr_{0.3}MnO_3$ Heterostructure. *JETP Lett.* **2014**, *99*, 27−31.

(18) Aspnes, D. Recombination at Semiconductor Surfaces and Interfaces. In *Surfaces and Interfaces: Physics and Electronics*; Elsevier, 1983; pp 406−421.

(19) Wen, X.; Chen, W.; Yang, J.; Ou, Q.; Yang, T.; Zhou, C.; Lin, H.; Wang, Z.; Zhang, Y.; Conibeer, G.; Bao, Q.; Jia, B.; Moss, d.J. Role of Surface Recombination in Halide Perovskite Nanoplatelets. *ACS Appl. Mater. Interfaces* **2018**, *10*, 31586−31593.

(20) Adhikari, N.; Dubey, A.; Khatiwada, D.; Mitul, A. F.; Wang, Q.; Venkatesan, S.; Iefanova, A.; Zai, J.; Qian, X.; Kumar, M.; Qiao, Q. Interfacial Study to Suppress Charge Carrier Recombination for High Efficiency Perovskite Solar Cells. *ACS Appl. Mater. Interfaces* **2015**, *7*, 26445−26454.

(21) Wu, S.; Wen, L.; Cheng, G.; Zheng, R.; Wu, X. Surface Morphology-Dependent Photoelectrochemical Properties of One-Dimensional Si Nanostructure Arrays Prepared by Chemical Etching. *ACS Appl. Mater. Interfaces* **2013**, *5*, 4769−4776.

(22) Galli, D.; Gasparini, N.; Forster, M.; Eckert, A.; Widling, C.; Killian, M. S.; Avgeropoulos, A.; Gregoriou, V. G.; Scherf, U.; Chochos, C. L.; Brabec, C. J.; Ameri, T. Suppressing the Surface Recombination and Tuning the Open-Circuit Voltage of Polymer/Fullerene Solar Cells by Implementing an Aggregative Ternary Compound. *ACS Appl. Mater. Interfaces* **2018**, *10*, 28803−28811.

(23) Glinka, Y. D.; Babakiray, S.; Johnson, T. A.; Bristow, A. D.; Holcomb, M. B.; Lederman, D. Ultrafast Carrier Dynamics in Thin-Films of the Topological Insulator Bi_2Se_3. *Appl. Phys. Lett.* **2013**, *103*, 151903.

(24) Lee, H.-S.; Park, H.-H. Band Structure Analysis of $La_{0.7}Sr_{0.3}MnO_3$ Perovskite Manganite Using a Synchrotron. *Adv. Condens. Matter Phys.* **2015**, *2015*, No. 746475.

(25) Bennett, B. R.; Soref, R. A.; Del Alamo, J. A. Carrier-Induced Change in Refractive Index of InP, GaAs and InGaAsP. *IEEE J. Quantum Electron.* **1990**, *26*, 113−122.

(26) Dai, Y. M.; Bowlan, J.; Li, H.; Miao, H.; Wu, S. F.; Kong, W. D.; Richard, P.; Shi, Y. G.; Trugman, S. A.; Zhu, J.-X.; Ding, H.; Taylor, A. J.; Yarotski, D. A.; Prasankumar, R. P. Ultrafast Carrier Dynamics in the Large-Magnetoresistance Material WTe_2. *Phys. Rev. B: Condens. Matter Mater. Phys.* **2015**, *92*, 161104.

(27) Sheu, Y. M.; Trugman, S. A.; Park, Y.-S.; Lee, S.; Yi, H. T.; Cheong, S.-W.; Jia, Q. X.; Taylor, A. J.; Prasankumar, R. P. Ultrafast Carrier Dynamics and Radiative Recombination in Multiferroic $BiFeO_3$. *Appl. Phys. Lett.* **2012**, *100*, 242904.

(28) Glinka, Y. D.; Babakiray, S.; Johnson, T. A.; Holcomb, M. B.; Lederman, D. Nonlinear Optical Observation of Coherent Acoustic

DOI: 10.1021/acsnano.8b09595
ACS Nano 2019, 13, 3457−3465

Dirac Plasmons in Thin-Film Topological Insulators. *Nat. Commun.* **2016**, *7*, 13054.
(29) Sundaram, S. K.; Mazur, E. Inducing and Probing Non-Thermal Transitions in Semiconductors Using Femtosecond Laser Pulses. *Nat. Mater.* **2002**, *1*, 217−224.
(30) Sheu, Y. M.; Chien, Y. J.; Uher, C.; Fahy, S.; Reis, D. A. Free-Carrier Relaxation and Lattice Heating in Photoexcited Bismuth. *Phys. Rev. B: Condens. Matter Mater. Phys.* **2013**, *87*, No. 075429.
(31) Ikezawa, M.; Pal, B.; Masumoto, Y.; Ignatiev, I. V.; Verbin, S. Y.; Gerlovin, I. Y. Submillisecond Electron Spin Relaxation in InP Quantum Dots. *Phys. Rev. B: Condens. Matter Mater. Phys.* **2005**, *72*, 153302.
(32) Giovanni, D.; Ma, H.; Chua, J.; Grätzel, M.; Ramesh, R.; Mhaisalkar, S.; Mathews, N.; Sum, T. C. Highly Spin-Polarized Carrier Dynamics and Ultralarge Photoinduced Magnetization in $CH_3NH_3PbI_3$ Perovskite Thin Films. *Nano Lett.* **2015**, *15*, 1553−1558.
(33) Yoshida, S.; Aizawa, Y.; Wang, Z.; Oshima, R.; Mera, Y.; Matsuyama, E.; Oigawa, H.; Takeuchi, O.; Shigekawa, H. Probing Ultrafast Spin Dynamics with Optical Pump−Probe Scanning Tunnelling Microscopy. *Nat. Nanotechnol.* **2014**, *9*, 588−593.
(34) Heers, S. Effect of Spin-Orbit Scattering on Transport Properties of Low-Dimensional Dilute Alloys. Ph.D. Dissertation. Forschungszentrum Jülich, 2011.
(35) Setyawan, W.; Curtarolo, S. High-Throughput Electronic Band Structure Calculations: Challenges and Tools. *Comput. Mater. Sci.* **2010**, *49*, 299−312.
(36) Maurice, J.-L.; Pailloux, F.; Barthélémy, A.; Durand, O.; Imhoff, D.; Lyonnet, R.; Rocher, A.; Contour, J.-P. Strain Relaxation in the Epitaxy of $La_{2/3}Sr_{1/3}MnO_3$ Grown by Pulsed-Laser Deposition on $SrTiO_3$ (001). *Philos. Mag.* **2003**, *83*, 3201−3224.
(37) Picozzi, S.; Ma, C.; Yang, Z.; Bertacco, R.; Cantoni, M.; Cattoni, A.; Petti, D.; Brivio, S.; Ciccacci, F. Oxygen Vacancies and Induced Changes in the Electronic and Magnetic Structures of $La_{0.66}Sr_{0.33}MnO_3$: A Combined *Ab Initio* and Photoemission Study. *Phys. Rev. B: Condens. Matter Mater. Phys.* **2007**, *75*, 094418.
(38) Gajdoš, M.; Hummer, K.; Kresse, G.; Furthmüller, J.; Bechstedt, F. Linear Optical Properties in the Projector-Augmented Wave Methodology. *Phys. Rev. B: Condens. Matter Mater. Phys.* **2006**, *73*, 1−9.
(39) Sandomirskii, V. Quantum Size Effect in a Semimetal Film. *Sov. Phys. JETP* **1967**, *25*, 158−166.
(40) Sichert, J. A.; Tong, Y.; Mutz, N.; Vollmer, M.; Fischer, S.; Milowska, K. Z.; García Cortadella, R.; Nickel, B.; Cardenas-Daw, C.; Stolarczyk, J. K.; Urban, A. S.; Feldmann, J. Quantum Size Effect in Organometal Halide Perovskite Nanoplatelets. *Nano Lett.* **2015**, *15*, 6521−6527.
(41) Trappen, R.; Garcia-Castro, A. C.; Tra, V. T.; Huang, C.-Y.; Ibarra-Hernandez, W.; Fitch, J.; Singh, S.; Zhou, J.; Cabrera, G.; Chu, Y.-H.; LeBeau, J. M.; Romero, A. H.; Holcomb, M. B. Electrostatic Potential and Valence Modulation in $La_{0.7}Sr_{0.3}MnO_3$ Thin Films. *Sci. Rep.* **2018**, *8*, 14313.
(42) Zu, F.; Amsalem, P.; Ralaiarisoa, M.; Schultz, T.; Schlesinger, R.; Koch, N. Surface State Density Determines the Energy Level Alignment at Hybrid Perovskite/Electron Acceptors Interfaces. *ACS Appl. Mater. Interfaces* **2017**, *9*, 41546−41552.
(43) Zhang, Z.; Yates, J. T. Band Bending in Semiconductors: Chemical and Physical Consequences at Surfaces and Interfaces. *Chem. Rev.* **2012**, *112*, 5520−5551.
(44) Lin, X. E. Laser Pulse Heating. *Proceeding of the 1999 Particle Accelerator Conference* **1999**, *3*, 1429−1432.
(45) Mottaghi, N.; Trappen, R. B.; Kumari, S.; Huang, C.-Y.; Yousefi, S.; Cabrera, G. B.; Aziziha, M.; Haertter, A.; Johnson, M. B.; Seehra, M. S.; Holcomb, M. B. Observation and Interpretation of Negative Remanent Magnetization and Inverted Hysteresis Loops in a Thin Film of $La_{0.7}Sr_{0.3}MnO_3$. *J. Phys.: Condens. Matter* **2018**, *30*, 405804.
(46) Müller, G. M.; Walowski, J.; Djordjevic, M.; Miao, G.-X.; Gupta, A.; Ramos, A. V.; Gehrke, K.; Moshnyaga, V.; Samwer, K.; Schmalhorst, J.; Thomas, A.; Hütten, A.; Reiss, G.; Moodera, J. S.; Münzenberg, M. Spin Polarization in Half-Metals Probed by Femtosecond Spin Excitation. *Nat. Mater.* **2009**, *8*, 56−61.
(47) Kresse, G.; Hafner, J. *Ab Initio* Molecular Dynamics for Liquid Metals. *Phys. Rev. B: Condens. Matter Mater. Phys.* **1993**, *47*, 558−561.
(48) Kresse, G.; Furthmüller, J. Efficient Iterative Schemes for *Ab Initio* Total-Energy Calculations Using a Plane-Wave Basis Set. *Phys. Rev. B: Condens. Matter Mater. Phys.* **1996**, *54*, 11169−11186.
(49) Perdew, J. P.; Ruzsinszky, A.; Csonka, G. I.; Vydrov, O. A.; Scuseria, G. E.; Constantin, L. A.; Zhou, X.; Burke, K. Restoring the Density-Gradient Expansion for Exchange in Solids and Surfaces. *Phys. Rev. Lett.* **2008**, *100*, 136406.
(50) Blöchl, P. E. Projector Augmented-Wave Method. *Phys. Rev. B: Condens. Matter Mater. Phys.* **1994**, *50*, 17953−17979.
(51) Kresse, G.; Joubert, D. From Ultrasoft Pseudopotentials to the Projector Augmented-Wave Method. *Phys. Rev. B: Condens. Matter Mater. Phys.* **1999**, *59*, 1758−1775.
(52) Bellaiche, L.; Vanderbilt, D. Virtual Crystal Approximation Revisited: Application to Dielectric and Piezoelectric Properties of Perovskites. *Phys. Rev. B: Condens. Matter Mater. Phys.* **2000**, *61*, 7877−7882.
(53) Pack, J. D.; Monkhorst, H. J. Special Points for Brillouin-Zone Integrations"-a Reply. *Phys. Rev. B* **1977**, *16*, 1748−1749.
(54) Liechtenstein, A. I.; Anisimov, V. I.; Zaanen, J. Density-Functional Theory and Strong Interactions: Orbital Ordering in Mott-Hubbard Insulators. *Phys. Rev. B: Condens. Matter Mater. Phys.* **1995**, *52*, R5467−R5471.
(55) Lee, J. H.; Delaney, K. T.; Bousquet, E.; Spaldin, N. A.; Rabe, K. M. Strong Coupling of Jahn-Teller Distortion to Oxygen-Octahedron Rotation and Functional Properties in Epitaxially Strained Orthorhombic $LaMnO_3$. *Phys. Rev. B: Condens. Matter Mater. Phys.* **2013**, *88*, 174426.
(56) Uba, L.; Uba, S.; Germash, L. P.; Bekenov, L. V.; Antonov, V. N. Electronic Structure and Magneto-Optical Spectra of $La_XSr_{1-X}MnO_3$ Perovskites: Theory and Experiment. *Phys. Rev. B: Condens. Matter Mater. Phys.* **2012**, *85*, 125124.
(57) Hibble, S. J.; Cooper, S. P.; Hannon, A. C.; Fawcett, I. D.; Greenblatt, M. Related Content Local Distortions in the Colossal Magnetoresistive Manganates La0.70Ca0.30MnO3, La0.80Ca0.20MnO3 and La0.70Sr0.30MnO3 Revealed by Total Neutron Diffraction. *J. Phys.: Condens. Matter* **1999**, *11*, 9221−9238.

DOI: 10.1021/acsnano.8b09595
ACS Nano 2019, 13, 3457−3465